

# High-Resolution Direct Numerical Simulations of Flow Structure and Aerodynamic Performance of Wind Turbine Airfoil at Wide Range of Reynolds Numbers

M. E. Nakhchi<sup>1</sup>, S. Win Naung, M. Rahmati

Faculty of Engineering and Environment, Northumbria University, Newcastle upon Tyne, NE1 8ST, UK

## Abstract

The objective of this study is to develop direct numerical simulations (DNS) to investigate the aerodynamic performance, transition to turbulence, and to capture the laminar separation bubble occurring on a wind turbine blade. Simulations are conducted with spectral/hp element method to investigate the details of flow separation bubble over wind turbine blades with NACA-4412 airfoil at wide range of design parameters. This airfoil is chosen because recent studies have shown that it is challenging to capture the details of the flow instabilities and pressure fluctuations in the separated shear layer of wind turbines by experimental methods. Furthermore, owing to more accurate development of DNS, the separated bubbles at high Reynolds numbers are captured. The results show that the vortex structures shed from the trailing edge of the airfoil by raising the angle of attack ( $\alpha$ ). Consequently, the fully turbulent flow develops downstream of the trailing edge (Karman vortex). Moreover, the pressure fluctuation significantly increased by raising  $\alpha$ . However, some rolling up of the flow structures, similar to Kelvin–Helmholtz rolls, on the pressure surface near the trailing edge, are observed at  $\alpha > 12^\circ$ . The separation point was delayed from  $X_{sep}/C=0.19$  to 0.58 by decreasing  $\alpha$  from 16 to 0 at  $Re=5\times 10^4$ .

**Keywords:** Direct numerical simulations; Wind turbine; Vortex shedding; Laminar separation bubble; Spectral/hp element method.

---

<sup>1</sup> Corresponding author ([mahdi.nakhchi@northumbria.ac.uk](mailto:mahdi.nakhchi@northumbria.ac.uk)), Tel: +447311486451

## 1. Introduction

Using wind energy is growing rapidly as a very popular and efficient source of renewable energy, because it is clean, and economical affordable. As a result, installation capacities of the wind turbines are increasing each year. Earlier low-fidelity computational methods such as Reynolds average Navier-Stokes (RANS) models have been widely used in the past decades to predict the flow behaviour and aerodynamic performance of the wind turbines. However, it is difficult and nearly impossible to capture the details of the transitional flows, pressure fluctuations and instabilities in the separated shear layer over the blades, which has significant impact on the performance of the wind turbines. Moreover, another disadvantage of the RANS models is their large computational resources requirement, and long runtimes of these methods [1]. The separation of boundary layer could make undesirable effects on the blade aerodynamic performance and could lead to blade oscillations, and noise generation. Therefore, it is important to accurately predict the flow structure and separating point over the wind turbine blade to increase the energy efficiency and the aerodynamics performance of the horizontal-axis wind turbines. Consequently, clean energy researchers tend to find the details of the flow structure and aerodynamic performance of the wind turbine blades to improve the efficiency at different transient physical conditions.

The separation of boundary layer from the surface of the wind turbine blades, is due to the presence of adverse pressure gradient on the suction surface of the blades. The adverse pressure gradient and the separated shear-layer depend on the flow regime, angle of attack (AoA), the shape of the airfoil, rotational speed and other physical parameters. The onset of transition to turbulence in the separated shear-layer is also another important parameter in the design of wind turbines. The variations of the angle of attack have considerable effect on flow disturbance intensification in the boundary-layer region. Accurate prediction of the onset of transition and the details of the velocity fluctuations on the wind turbine blades is still an

important challenging problem for the designers. Naung et al. [1] numerically examined the effects of the flow unsteadiness on the flow separation and aeroelastic behaviour of the wind turbine blades. They found that the inlet wakes have substantial effect on wind turbine aerodynamics and separation point. In another numerical study, Naung et al. [2, 3] utilized the frequency-domain method to predict the forced response and flutter instability over the wind turbine blades. They concluded that by using the newly designed model, the computation time can be reduced by order of 2 compared to the other models. The effects of the inner blade phase angle on the separation point and vortex generation in the wake region were also investigated. In a recent numerical study, Zhang et al. [4] numerically investigated the effects of a newly designed winglet on the power efficiency of the vertical-axis wind turbines. They observed that the winglets improve the efficiency of the wind turbines by separating the pressure side and the suction side of the blade and keeping the pressure difference on the blade surface. The tip-vortex variations due to the winglet vortex generators were also investigated.

The area that has recirculation flows and vortex generations is generally called Separation Bubble [5]. Koca et al. [6] experimentally investigated the vortex generation over NACA-4412 wind turbine airfoil. The effect of Reynolds number and angle of attack on the recirculations flows and laminar separation bubble was investigated. They used hot-film with glue on-probe technique to visualize the flow streamlines over the wind turbine blade. They concluded that LSB moved near to leading edge of the aerofoil as the Reynolds number was enhanced from  $2.5 \times 10^4$  to  $7.5 \times 10^4$  and smaller laminar separation bubbles (LSB) generated at lower angle of attack. Xu et al. [7] performed numerical simulations on the aerodynamic performance of vertical-axis wind turbine blade sections. They used winglets to improve the performance of the performance of the wind turbine. They found that the power coefficient can be increased by 19% by using winglet vortex generators with the same swept areas. In the numerical study of Zhang et al. [8], the authors employed various NACA airfoils to find the best configuration

of the vertical-axis wind turbine blades. Their three-dimensional simulations revealed that the NACA-0018 aerofoils with the pitch angle of  $6^\circ$ , performs the best between all the airfoils with different thickness. It was found that the flow separation occurs earlier over thinner aerofoils than the thicker ones by raising the angle of attack. Açıkel and Genç [9] used a partially flexible membrane to control the flow separation over NACA-4412 wind turbine airfoil at low Reynolds numbers. Their experimental analysis revealed that the LSB on surface was suppressed by using the membranes. Moreover, the lift coefficient was increased while drag was reduced, but stall performed early at  $\alpha = 10^\circ$ . Kamada et al. [10] used oil-film method, and blade surface tufts to visualise the flow structure over horizontal-axis wind turbine airfoils. The Separation bubbles were presented for the case of turbulent intensity (TI)=0.20% and  $Re=2.0 \times 10^5$ . The experiments showed that when the angle of attack increased, the separated region and vortex generations become larger and noticeable. Ou et al. [11] performed a detailed parametric study on drag reduction of turbulent flows in a combinational system. They found that the proposed numerical model can accurately predict the flow structure in the opposing jet protection systems. In another numerical study, Huang et al. [12] investigated the impact of different turbulent models and the slot width on the pressure coefficient variations in subsonic air flows. They concluded that the SST  $k-\omega$  turbulence model can predict the details of the flow structure in the separated regions. Rezaeiha et al. [13] used active flow control techniques to improve the performance of vertical-axis wind turbines. The high-fidelity numerical analysis shows that applying suction ahead the chord length of the laminar separation bubble can avoid its bursting, delay the formation of LSB, and prevent the formation of the trailing-edge roll-up vortex over the airfoil section.

D'Alessandro et al. [14] used Large eddy simulations (LES) to predict the flow structure and control the separation over dimpled wind turbine blade with NACA 64-014A airfoil. The simulations were performed at  $Re=1.75 \times 10^5$ . They found that the dimples produce a reduction

of the LSB extension if the dimples were positioned before the LSB. The effects of the trailing edge cutback on a turbine blade was numerically investigated by Moriguchi et al. [15]. They concluded that thickness of the boundary layer, and the pressure fluctuations have been influenced by the cutbacks. Naung et al. [16] employed direct numerical simulations (DNS) to predict the interactions among the transitional flow and the blades oscillations of the low-pressure turbines. They found that typical unsteady Reynolds Averaged Navier–Stokes (URANS) models cannot capture the velocity and pressure fluctuations and separation point over the turbine airfoils. Moreover, they concluded that the harmonic balance method needs much less computation times compared to the time domain method.

Accurate prediction of the turbulent fluctuations at different air velocities and angles of attack (AoA) can help to predict the aerodynamic performance of the wind turbines and to reduce or prevent flow separation. Moreover, LSB formation, stall prediction, and control the flow structure is an important topic among the wind turbine designers. Saleem and Kim [17] numerically investigated the effect of tip clearance on the aerodynamic performance of the wind turbines. They used NACA-9415 airfoil for the numerical simulations over the wind turbine blade section. They found that the blad tip gaps can increase the power coefficient for 25m/s wind speed. Based on the recent numerical and experimental studies in the field of fluid dynamics of wind turbine airfoils, it was found that the LSB formation and wind turbine performance depends on the value of the angle of attack [18], physical parameters such as Reynolds number [19] and the shape of the blade airfoil [20].

Wahidi et al. [21], used particle image velocimetry (PIV) technique to visualize the flow structure and laminar separation bubble over NACA4412 blade. The experiments showed that the flow separating point and instantaneous reattachment of the flow over the blade surface depended on the angle of attack. They concluded that some pairs of forward and backward velocity were generated in the separated region. These pairs have significant impact on the

velocity fluctuations in the reattachment areas. Cui et al. [22] applied the delayed detached eddy simulation based upon the  $k-\omega-\gamma$  transition/turbulence integration method (IDDES-Tr) to investigate the separation flow structure over wind turbine airfoil. They found that the proposed model can detect more details of the flow behaviour over the wind turbine compared to large eddy simulation (LES) method. O'meara and Mueller [23] experimentally investigated the LSB over NACA 663-018 airfoil at Reynolds number is the range of  $5 \times 10^4$  to  $2 \times 10^5$  and ( $8^\circ < \alpha < 12^\circ$ ). They found that the thickness of LSB decreased by raising the Reynolds number. Moreover, raising the angle of attack would also increase the thickness and the size of LSB over the airfoil. In the numerical study of Alam and Sandham [24], three-dimensional simulations were performed to investigate the LSB and the onset of transition over the blade airfoil. They found that the bubbles with turbulent reattachment have maximum reverse flows of less than 8%. It was also concluded that the basic instability source is convective in these separated bubbles. Transition onset was detected by experiencing the Kelvin–Helmholtz instabilities in the separated shear-layer.

Spectral/hp element method is a novel and highly precise and computational efficient DNS method that includes the advantages of typical finite element techniques alongside spectral element methods. By utilizing this procedure, the computation performance can be substantially decreased whilst the precision stays high and even be enhanced in comparison with other DNS techniques. This method is originally established by Karniadakis and Sherwin [25] concerning aerodynamics and incompressible fluid mechanics. This highly accurate method can be utilized in three-dimensional studies over turbine blades with higher efficiencies. This approach can also be employed to catch the transient flow structure and pressure fluctuations in separated flow regions at moderate-high Reynolds numbers [26]. The applications of this method is recently expanded in the study of Moxey et al. [27] to better capture the spatially-varying flow perturbations. Bao et al. [28], used spectral/hp element

method to calculate the transient flow perturbations and separation flow over a vibrating cylinder. They found that the vortex induced oscillations at  $Re=3,900$  can alter the flow structure over the riser. The drag and lift coefficient were also captured at different time steps. Recently, Cassinelli et al. [29] used this method to analyse the flow behaviour, separating points and friction coefficient over a turbine cascade at specific Reynolds number. Excellent agreement was observed between the DNS results and experiments for the pressure coefficient at  $Re=160,000$ . The study was concentrated on the dynamics of the separation bubble on the suction surface of the blade. However, this highly accurate and computationally efficient method has not been previously utilized to calculate the flow structure over wind turbine blades.

The above literature review show that it is essential to predict the flow separation and the vortex generations over the wind turbine airfoils at different Reynolds numbers and angle of attacks. However, most of the recent studies were focused on experimental investigations, and only a few numerical methods have been utilized to predict the flow structure and LSB over wind turbines. Moreover, there are no DNS studies to accurately predict the transitional flow structure over the NACA-4412 wind turbine blade section at high angle of attacks ( $\alpha > 12^\circ$ ). This motivated us to employ the spectral/hp element method for the DNS simulations at wide range of design parameters over the wind turbine airfoil. This numerical work is based on the recent experimental study of Koca et al. [6] to predict the details of the pressure fluctuations and flow unsteadiness which are not possible to be captured in experiments. As discussed later, the details of the flow separation and recirculations were not predicted accurately in the experiments. Moreover, the experimental data are limited to  $Re=5 \times 10^5$  and in this study, much higher Reynolds numbers are considered in the direct numerical simulations for the first time. Highly accurate numerical simulations over NACA-4412 airfoil based on spectral/hp element method are performed to predict the aerodynamic performance over the wind turbine section

at wide range of design parameters. In our study the Reynolds number in the range of  $2.5 \times 10^4 < Re < 1.5 \times 10^5$  and the angle of attack is varied from 0 to 16 degree. The main advantages of the proposed numerical model are (1) more accurate prediction of the separation point, vortex generation and recirculation flows at different flow conditions, (2) significant reduction in computational times compared to the previous models, and (3) analysing the instantaneous and time-averaged wake profiles and pressure coefficients and aerodynamic parameters over the wind turbine section at different angle of attacks.

## 2. Physical and mathematical modelling

### 2.1. Problem description

Figure 1 shows the section view of the wind turbine blade with NACA-4412 airfoil. The blade aspect ratio is  $\Lambda = 4.53$ , the chord length is  $C = 0.225$  m and spanwise size is  $L_z = 0.2-0.5$  m. The blade installation angle of attack ( $\alpha$ ) is varied between 0 to 16 degree in the present DNS study. The inlet velocity is uniform and the Reynolds number ( $Re = U_0 C / \nu$ ) is varied between 25,000 and 150,000.

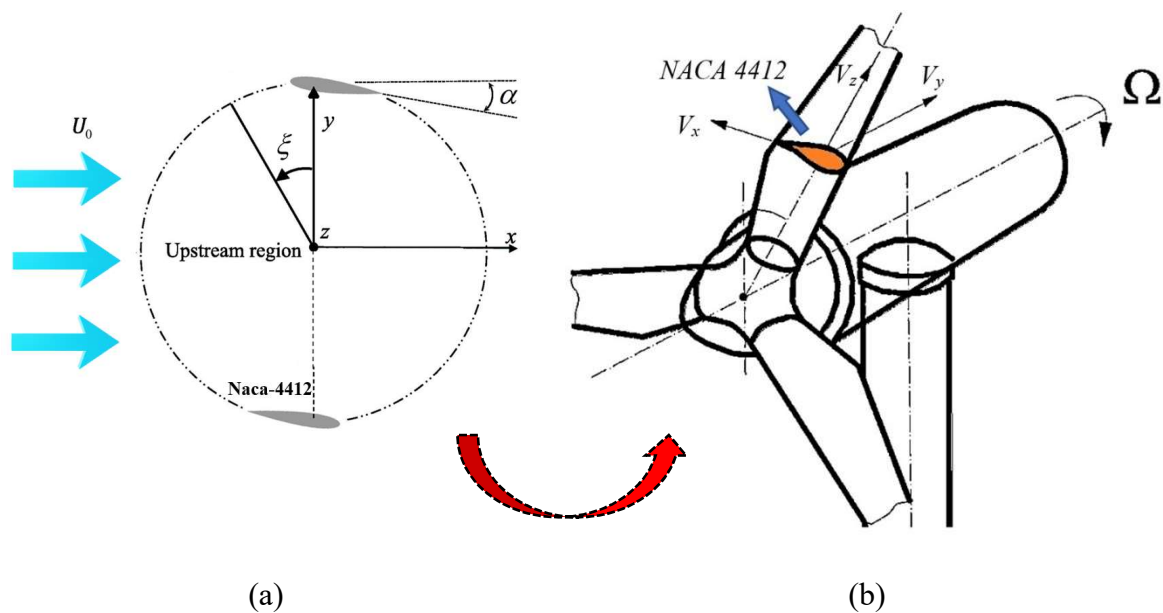


**Fig. 1** (a) Schematic view of the wind turbine blade with NACA4412 airfoil mid-section, (b) the details of the geometrical parameters.

## 2.2. Governing equations

The three-dimensional transient, and incompressible momentum and continuity Navier-Stokes equations in the dimensionless type utilized in the current study are as follows:

$$\frac{\partial \mathbf{u}}{\partial t} + (\mathbf{u} \cdot \nabla) \mathbf{u} = -\nabla p + \nu \nabla^2 \mathbf{u} \quad (1)$$

$$\nabla \cdot \mathbf{u} = 0 \quad (2)$$

where vector  $\mathbf{u}=(u,v,w)$  shows the air flow velocity,  $p$  is the dynamic pressure, and  $\nu$  is the kinematic viscosity of the working fluid.

The Spectral/hp element procedure can utilize a 2D mesh and the simulations could be extended in the span direction by applying the Fast Fourier Transform. This method is very efficient to precisely detect the separated shear layer, onset of transition, vortex production and details of the pressure fluctuations over at different angle of attacks and different Reynolds numbers, especially in wind turbines that the details of the flow structure and laminar separation bubble need to be predicted accurately. This method is currently accessible in an open-source code called NEKTAR++.

Figure 2 shows the simulation algorithm and the relationship among the local and mapped regions by using the MPI communicator. The domain decomposition and modal/nodal expansions can be linked to each other via the mapping function. The applications of the mapping function in time-dependent turbulent flows can expressed by the following function:

$$\mathbf{u}^\delta(x_1, x_2) = \sum_{\varepsilon=1}^N \left( \sum_{p=0}^{P_1} \left( \sum_{q=0}^{P_2} \hat{\mathbf{u}}_{pq}^\varepsilon(x_1, x_2) \right) \right) \quad (3)$$

The goal is to calculate the terms of  $\hat{u}_{pq}^\varepsilon$  by using the spectral/hp element method. Determining the Advection, Poisson, and Helmholtz terms in the solution algorithm, need more computing times as compared to other sections in the transient discontinuous Galerkin method. The mapping function is used to distort the local mesh  $(x_1, x_2)$  into rectangular elements  $(\xi_1, \xi_2)$  in the mapped coordinate system. The specifics of the mesh deformation are available in [30].

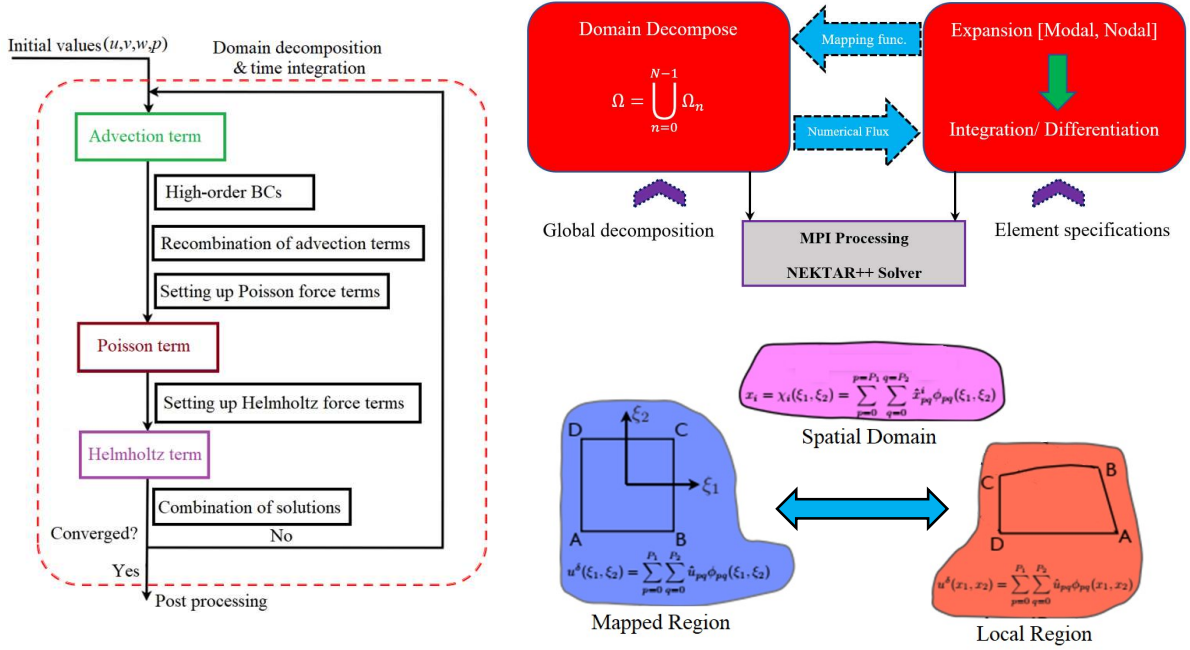


**Fig. 2** Simulation algorithm of the high-resolution spectral/hp element method over wind turbine blade with mapping functions.

This method has the options to select continuous Galerkin (CG) and discontinuous Galerkin (DG) schemes are applicable in the solver [31]. In this study, discontinuous Galerkin (DG) method is selected for the DNS simulations over the wind turbine blade. Based on the DG method, the momentum equation can be stated as:

$$\frac{\partial \mathbf{u}}{\partial t} = \mathbf{N}(\mathbf{u}) - \nabla p + \nu \mathbf{L}(\mathbf{u}) \quad (4)$$

where  $\mathbf{N}(\mathbf{u}) = -(\mathbf{u} \cdot \nabla) \mathbf{u}$  is the nonlinear convective term, and  $\mathbf{L}(\mathbf{u}) = \nabla^2 \mathbf{u}$  is the viscous term, respectively. By using the time-integration method of Karniadakis et al. [32], the above

equation can be discretized by utilizing backward differentiation formulation. By discretizing the nonlinear convection phrase with polynomial extrapolation from prior time steps, the momentum equation at  $\delta t^* = n + 1$  will be stated as:

$$\frac{\lambda_0 \mathbf{u}^{n+1} - \sum_{m=0}^{J_i-1} \alpha_m \mathbf{u}^{n-m}}{\Delta t} = \sum_{m=0}^{J_e-1} \beta_m \mathbf{N}(\mathbf{u}^{n-m}) - \nabla p^{n+1} + \nu \mathbf{L}(\mathbf{u}^{n+1}) \quad (5)$$

In which  $J_e$  and  $J_i$  are the integration orders of the explicit and implicit phrases and  $\alpha$ ,  $\beta$  and  $\lambda$  are the equation factors. The Eq. (5) can be shortened by:

$$\frac{\lambda_0 \mathbf{u}^{n+1} - \mathbf{u}^*}{\Delta t} = N^* - \nabla p^{n+1} + \nu \mathbf{L}(\mathbf{u}^{n+1}) \quad (6)$$

where  $\mathbf{u}^* = \sum_{m=0}^{J_i-1} \alpha_m \mathbf{u}^{n-m}$  and  $N^* = \sum_{m=0}^{J_e-1} \beta_m \mathbf{N}(\mathbf{u}^{n-m})$ . Based on the Guermond and Shen's approach

[33], and with integration over the domain, we have:

$$\int_{\Omega} \nabla p^{n+1} \cdot \nabla \phi d\Omega = \int_{\Omega} \left( \frac{\mathbf{u}^* - \gamma_0 \bar{\mathbf{u}}^{n+1}}{\Delta t} + N^* - \nu (\nabla \times \nabla \times \mathbf{u})^+ \right) \cdot \nabla \phi d\Omega \quad (7)$$

In which  $\nabla \phi$  is a flow function in the computation domain  $\Omega$ . The details of the simulation algorithm according to the Discontinuous Galerkin (DG) scheme are presented in Figure 2. More specifics about the the simulation method and discretization of the Advection, Poisson and Helmholtz terms are available in the Ref. [31].

The details of the mesh generation over the NACA-4412 airfoil in spectral/hp element method for the polynomial order of the 6 (P=6) are presented in Figure 3. Using polynomial order of 6 indicates that each element is separated in 6 sections at each side. Boundary-layer mesh with 8 inflated layers with the minimum size of 0.005m for the nearest layer with the growth rate of 1.1 are selected for the DNS computations over the wind turbine mid-section airfoil. It was observed that using 32 FFT planes in the span-direction would be enough for accurate prediction of the flow structure and instantaneous vortex generation isosurface.

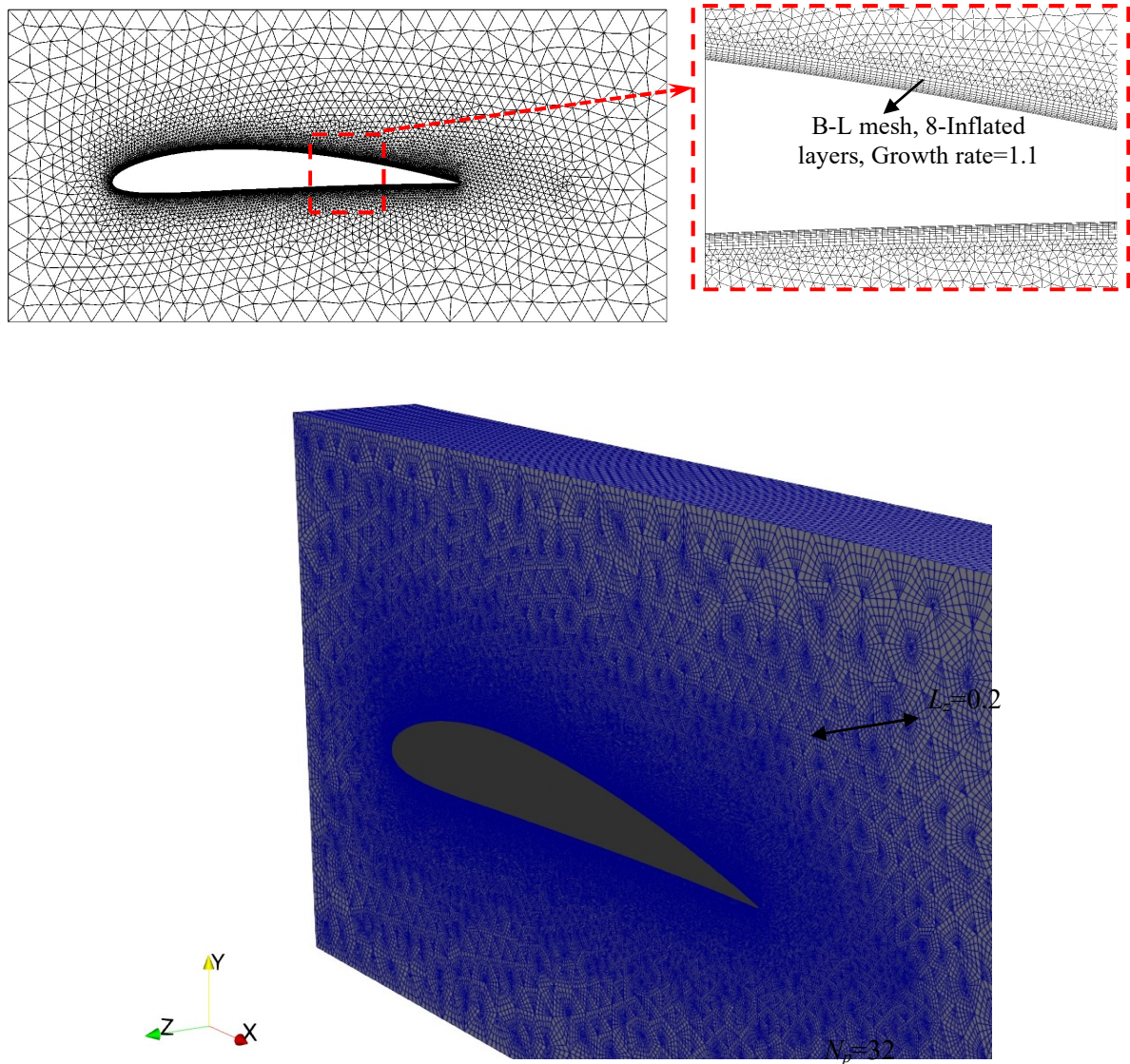


**Fig. 3** Mesh generation over the NACA-4412 airfoil in spectral/hp element method (P=6)

To ensure the accuracy of the computational domain, a grid independency study must be performed before the main DNS computations. The separation point ( $X_{sep}/C$ ) on the suction surface over the wind turbine blade was calculated at  $Re=150,000$  and  $AoA=16^\circ$  to select the most appropriate and accurate polynomial order for further calculations. The values of these parameters are reported in Table 1. It is observed that the deviations were significantly decreased by increasing P from 4 to 10. The relative deviation between P=10 and 12 for all of the evaluated parameters is the smallest. This indicates that P=10 is accurate enough (maximum deviation of 0.7%) to be used for post-processing and analysing of the computational results.

Consequently, P=10 was chosen for additional simulations on the wind turbine blade cascade with different geometrical and physical parameters.

**Table 1** Grid independence study for different polynomial orders at Re=150,000 and AoA=16°.

Polynomial order	$X_{sep}/C$	Deviation (%)
P=4	0.198	21.7
P=6	0.155	5.2
P=8	0.147	4.8
P=10	0.141	0.7
P=12	0.140	-

To make sure about the accuracy of the mesh generation near the walls of the wind turbine airfoil for a fully resolved DNS, it is necessary to capture the wall distances in all the cartesian directions over the blade suction surface and pressure surface. The wall<sup>+</sup> values must meet the following limitations [18]:  $\Delta x^+ < 20$ ,  $\Delta y^+ < 1$ , and  $\Delta z^+ < 10$ . The “+” sign denotes the scaling with the viscous length  $L^* < \nu/u_\tau$  and  $\nu$  is the kinematic viscosity of the air and  $u_\tau = \sqrt{\tau_w/\rho}$  is the frictional velocity. The wall<sup>+</sup> values over the suction surface of the NACA-4412 wind turbine blade at Re=150,000 and AoA=16° with  $P = 10$ ,  $L_z = 0.2$ ,  $Np = 96$  are presented in Figure 4. It can be seen that all the wall scale parameters in x, y, and z directions in the chord direction over the blade are in the eligible regions for each parameter. This means that the mesh generation is sufficiently accurate to find the separation and pressure fluctuations over the wind turbine blade.

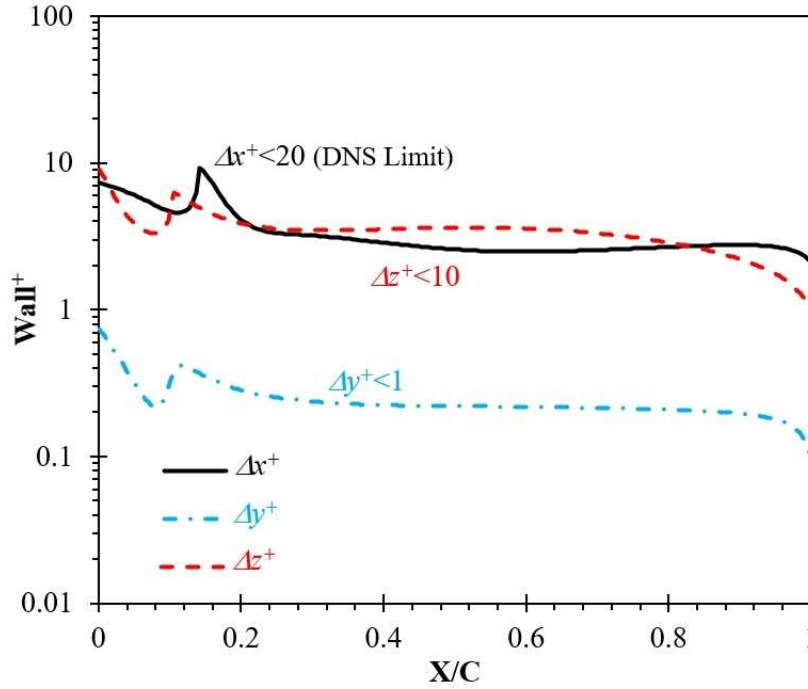
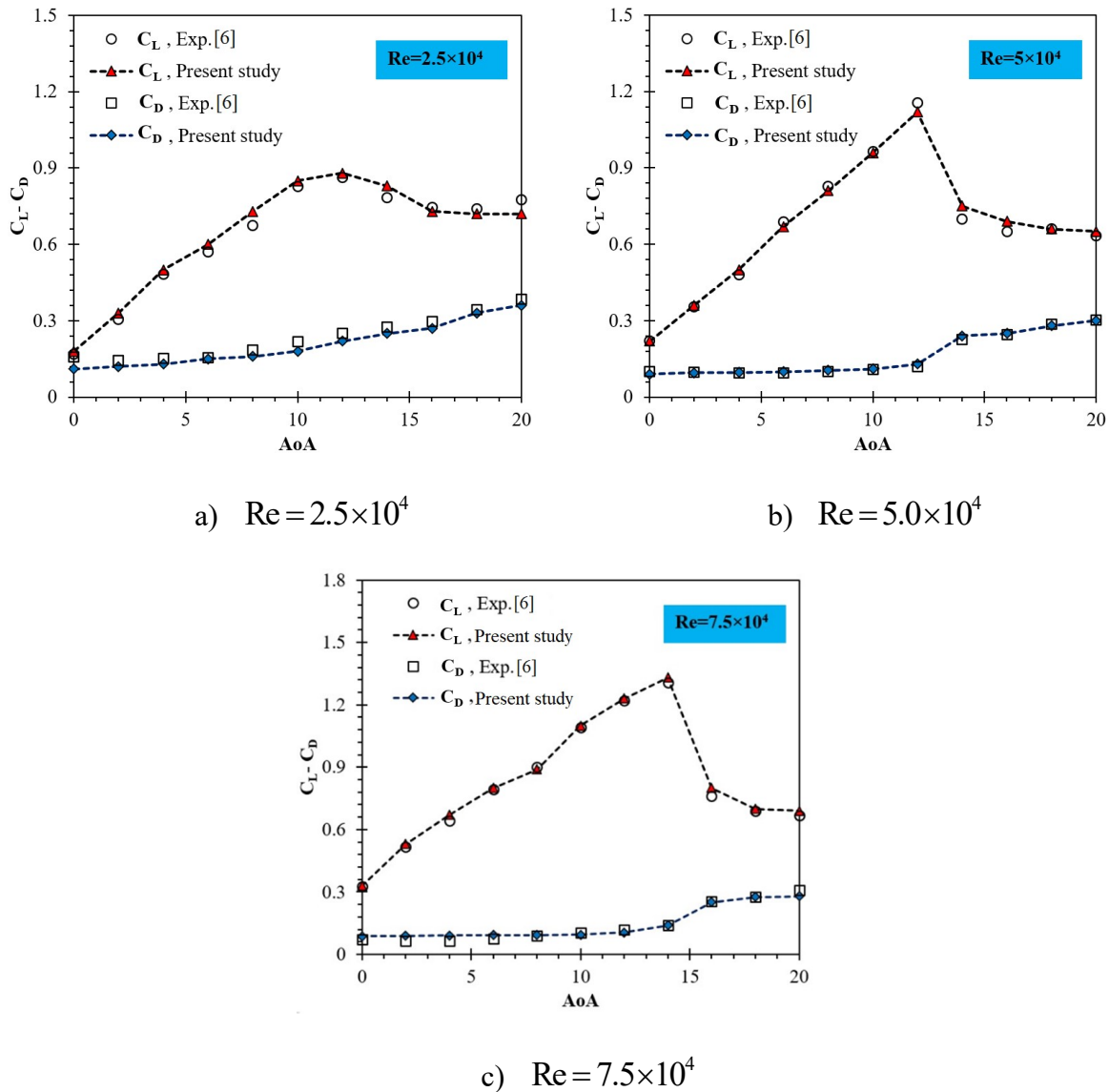


**Fig. 4** Near wall mesh resolution for  $P = 10$ ,  $Lz = 0.2$ ,  $Np = 96$  at  $Re=50,000$   $AoA=16$ .

### 3. Results and discussion

The numerical model and method employed in this study are first validated against the experiment [6] to ensure the accuracy. Figure 5 presents the comparison of the Drag-Lift coefficients with respect to the angle of attack (AoA) at various Reynolds numbers. As expected, the lift coefficient increases as the angle of attack rises until it reaches the maximum at the stall angle. The stall occurs at the  $AoA=12$  degrees at Reynolds numbers of  $2.5 \times 10^4$  and  $5 \times 10^4$ . However, the stall is delayed, and the stall angle is shifted to 14 degrees when the Reynolds number is increased to  $7.5 \times 10^4$  as the flow separation becomes smaller at higher Reynolds numbers. The maximum lift coefficients for Reynolds numbers of  $2.5 \times 10^4$ ,  $5 \times 10^4$  and  $7.5 \times 10^4$  are approximately 0.9, 1.2 and 1.3, respectively. Lift coefficient drops beyond the stall angle due to the flow separation and formation of the separation bubbles on the suction surface. The drop is more sudden and significant at higher Reynolds numbers. The aerodynamic performances in the post-stall region are dramatically reduced. The drag coefficient stays relatively flat until the stall angle and then it increases slightly after the stall

angle. For all Reynolds numbers, the results from the present DNS simulations are in excellent agreement with the experiment at all angles of attack. Therefore, it can be concluded that the present DNS simulation predicted the force applied on the aerofoil surfaces accurately.



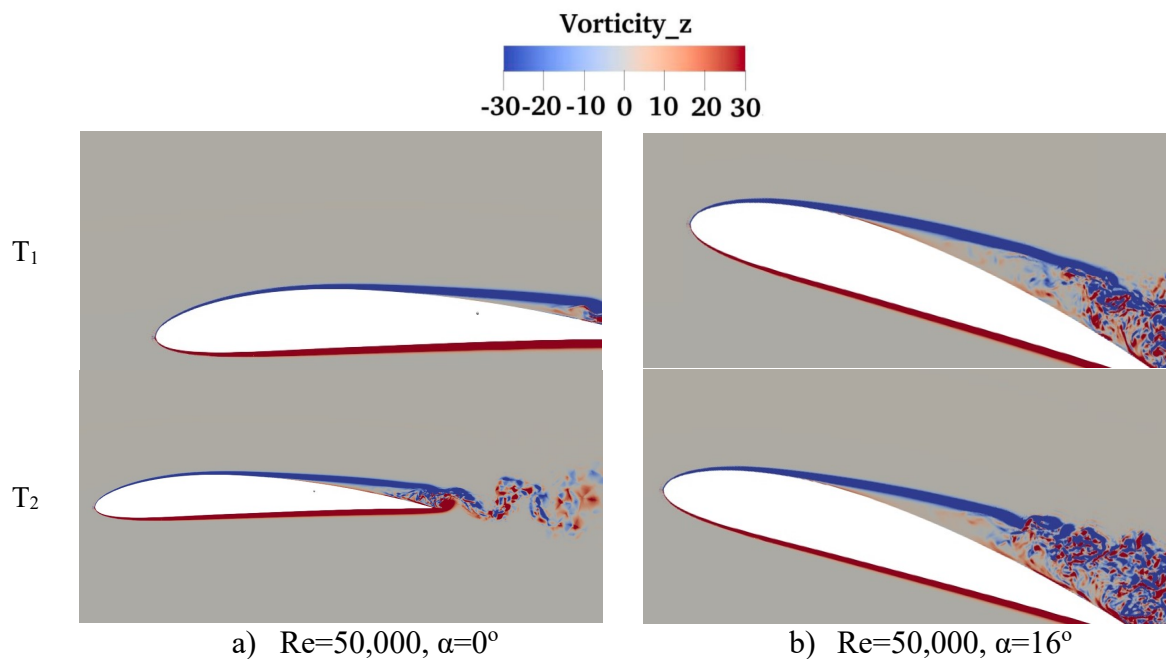
**Fig. 5** Validation of DNS results with experiments [6] at different Re numbers and AoAs.

Figure 6 illustrates the instantaneous vorticity contours at different angles of attack for the Reynolds numbers of  $5 \times 10^4$  and  $1.5 \times 10^5$ . The vorticity contours at the angles of attack of 0 degree and 16 degree are shown to highlight the differences in flow behaviour at relatively low and high angles of attack. At  $\alpha=0^\circ$ , the flow remains attached on the pressure surface and separates from the suction surface when the Reynolds number is  $5 \times 10^4$ , and the flow

recirculation and separation bubbles are developed on the suction surface before shedding from the trailing edge. The flow separation and vortex generation process continue as time goes on, and the vortex structures shed from the trailing edge of the aerofoil. As a result, the fully turbulent flow develops downstream of the trailing edge. The flow structures shed from the trailing edge are similar to those of Karman vortex. It is understood from the Drag-Lift coefficients in Fig. 3 that the stall angle is 12 degrees at the Reynolds number of  $5 \times 10^4$ . Therefore, the angle of 16 degrees falls within the post-stall region. At this relatively high angle of attack, the flow separation on the suction surface is much larger than that of the pre-stall region and the flow separation point moves towards the leading edge. Due to its large flow separation, the highly unsteady and strong vortex generation is observed on the suction surface near the trailing edge, which adds more turbulence to the downstream flow and vortex structures. The flow unsteadiness and turbulence become higher with the increasing time intervals as the separation bubbles move towards the leading edge along the suction surface.

The investigation of the flow structures for the Reynolds number of  $1.5 \times 10^5$  is particularly added to analyse and highlight the effect of Reynolds number on the formation of vortex structures and flow separation process. Compared to the Reynolds number of  $5 \times 10^4$ , the flow separation is much smaller in this case at both relatively low and high angles of attack due to its larger Reynolds number or, in other words, higher wind speed. At the angle of attack of 0 degree, the flow is mostly attached on the pressure surface; however, it is interesting to observe some small rolling up of the flow structures, similar to Kelvin–Helmholtz (KH) rolls, on the pressure surface near the trailing edge, which then combine with those from the suction surface and shed from the trailing edge. On the suction surface, the flow separates near the trailing edge; however, the flow separation is very small compared to that of Reynolds number of  $5 \times 10^4$ . The rolling up of the separated shear layer and flow recirculation are seen near the trailing edge. Then, they combine with flow structures from the pressure surface and the vortex

shedding occurs from the trailing edge of the aerofoil. It is noticed that the frequency of the vortex shedding is smaller than that of Reynolds number of  $5 \times 10^4$ . The boundary layer separation is slightly higher at  $\alpha=16^\circ$ . The separation point moves towards the leading edge and the flow separates from approximately half of the chord length. The flow recirculation and separation bubbles are observed on the suction surface, which then drop from the aerofoil surface and leave from the trailing edge adding more turbulence to the flow. A significant difference between the two Reynolds numbers is observed at  $\alpha=16^\circ$  as the flow separation at this angle is remarkably small when the Reynolds number is increased to  $1.5 \times 10^5$ . For a given adverse pressure gradient distribution, the separation resistance of the turbulent boundary layer increases with increasing Reynolds number. It can also be said that raising Reynolds number delays the stall as the stall phenomena does not occur at 16 degrees angle when Reynolds number is  $1.5 \times 10^5$ . This observation is consistent with the experiment in which it was seen that the stall angle moves to 14 degrees from 12 degrees when Reynolds number is increased to  $7.5 \times 10^4$  from  $5 \times 10^4$  (See Fig. 3). Similar to the 0-degree angle of attack, the vortex shedding frequency is also smaller with the higher Reynolds number.



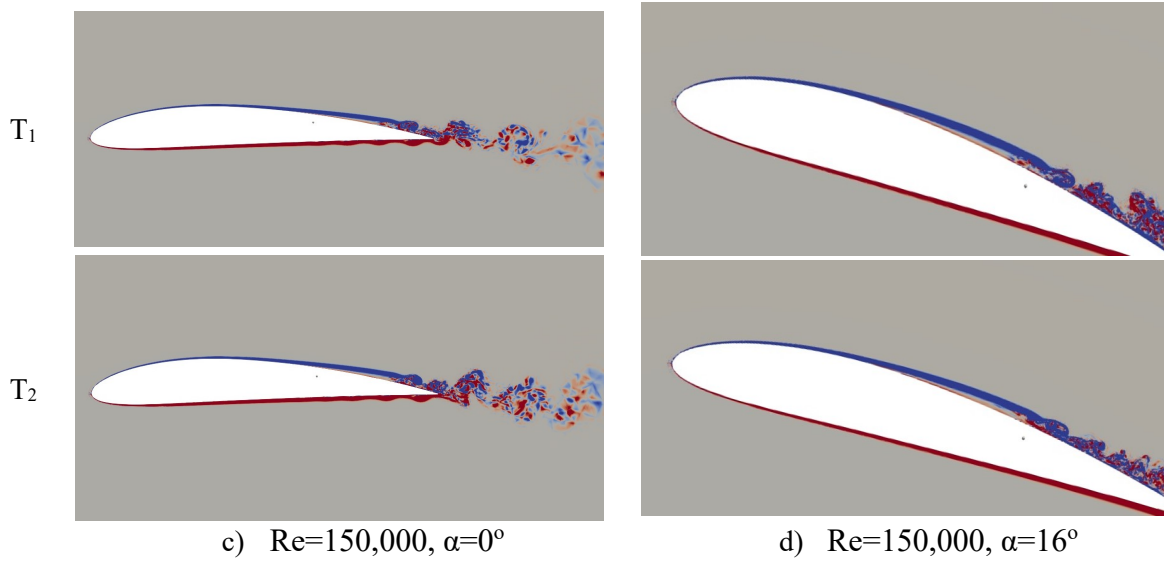
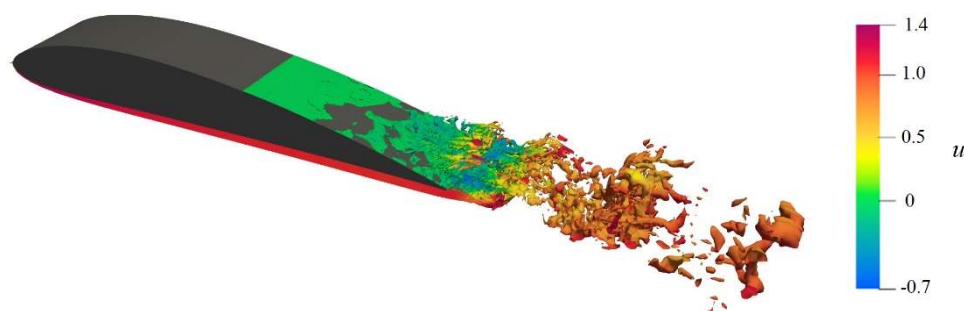


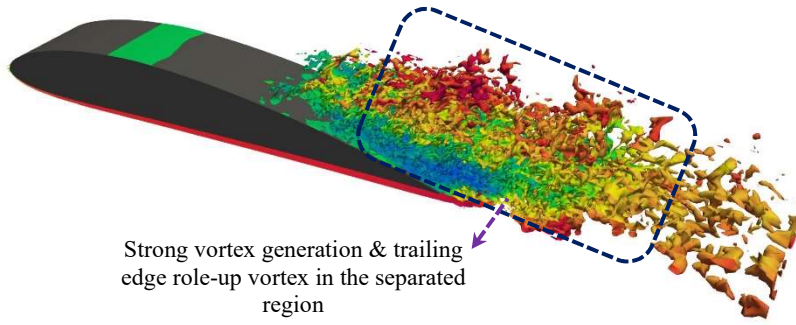
**Fig. 6** Instantaneous vorticity contours over the NACA-4412 at different Re numbers and AoAs.

The iso-surfaces of the axial vorticity for the angles of attack of 0 degree and 16 degrees at different Reynolds number including  $5 \times 10^4$ ,  $7.5 \times 10^4$  and  $1.5 \times 10^5$  are shown in Figure 7. The vorticity structures are made visible using the function of the flow velocity. At the Reynolds number of  $5 \times 10^4$ , the flow separates from  $X/C = 0.58$  when the angle of attack is 0 degree whereas the flow separation points move to  $X/C = 0.19$  at  $\alpha = 16^\circ$ . A large flow separation occurs near the leading edge at the 16-degree angle of attack, and the flow recirculation and the strong generation of vortex structures can be seen within the separation zone on the suction surface. Compared to the 0-degree angle of attack at which the vorticity structures are developed near the trailing edge, the flow is highly distorted, and the turbulence is amplified by the flow separation at  $\alpha = 16^\circ$ . However, the size of the flow separation is reduced at both angles of attack when Reynolds number is increased to  $7.5 \times 10^4$  as the higher wind speed increases the separation resistance of a turbulent boundary layer. The flow separation point is also delayed by increasing Reynolds number as it moves in the direction of the trailing edge to  $X/C = 0.39$  and  $X/C = 0.17$  at the 0-degree and 16-degree angles of attack, respectively. Formation of the Laminar Separation Bubble (LSB) and vortex structures and trailing edge role-up vortex can be seen on the suction surface leading to the laminar to turbulence transition near the trailing

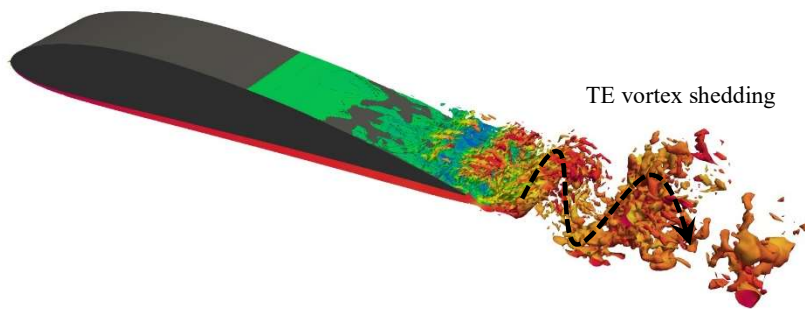
edge. The vortex structures break down into smaller structures as they shed away from the trailing edge. In contrast to the Reynolds number of  $5 \times 10^4$ , the sizes of the vortex structures are smaller at this Reynolds number. Interesting flow structures are observed if Reynolds number is further increased to  $1.5 \times 10^5$ . Although the flow is mostly attached on the pressure surface at the angle of attack of 0 degree, some small rolling up of the wavy flow structures, similar to KH rolls, are seen near the trailing edge. At the 16-degree angle of attack, the flow separation is very small compared to that of the other two Reynolds numbers. The turbulent boundary layer becomes uniform due to the higher wind speed. The flow separation point moves slightly towards the trailing edge as the flow separates from  $X/C = 0.30$  and  $X/C = 0.14$  at the angles of attack of 0 degree and 16 degrees, respectively. The flow separation points for different Reynolds number and angles of attack are presented in Table 2. It is seen that the flow separation point moves towards the leading edge when increasing the angle of attack whereas the separation is delayed and the separation point moves in the direction of trailing edge when increasing the Reynolds number. The higher wind speed intensifies the formation of separation bubbles and generation of vortex structures which make the flow more unsteady and turbulent. However, the vorticity structures downstream of the trailing edge are also smaller at this Reynolds number than the other two cases. The conclusions can be drawn from these observations that the size of flow separation can be reduced by increasing Reynolds number which, at the same time, triggers stronger separation bubbles and vortex generation that amplify flow disturbances and turbulence downstream of the trailing edge.



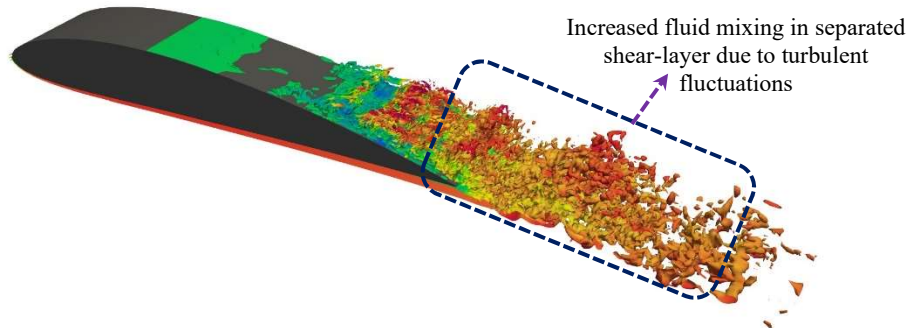
a)  $Re=5 \times 10^4, \alpha=0^\circ$



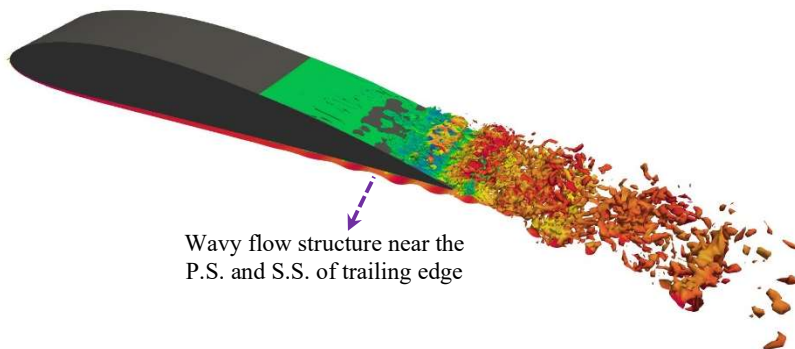
b)  $Re=5 \times 10^4, \alpha=16^\circ$



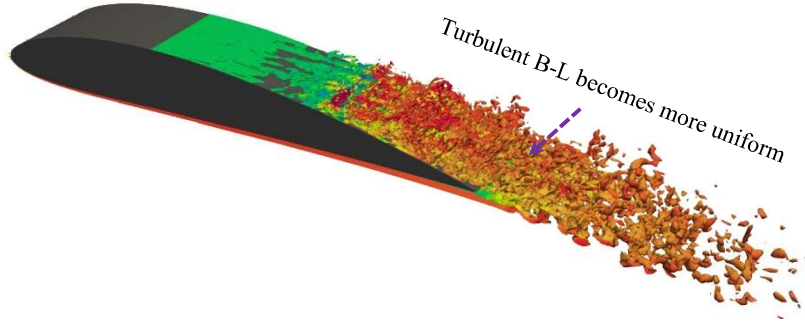
c)  $Re=7.5 \times 10^4, \alpha=0^\circ$



d)  $Re=7.5 \times 10^4, \alpha=16^\circ$



e)  $Re=1.5 \times 10^5, \alpha=0^\circ$



f)  $Re=1.5 \times 10^5$ ,  $\alpha=16^\circ$

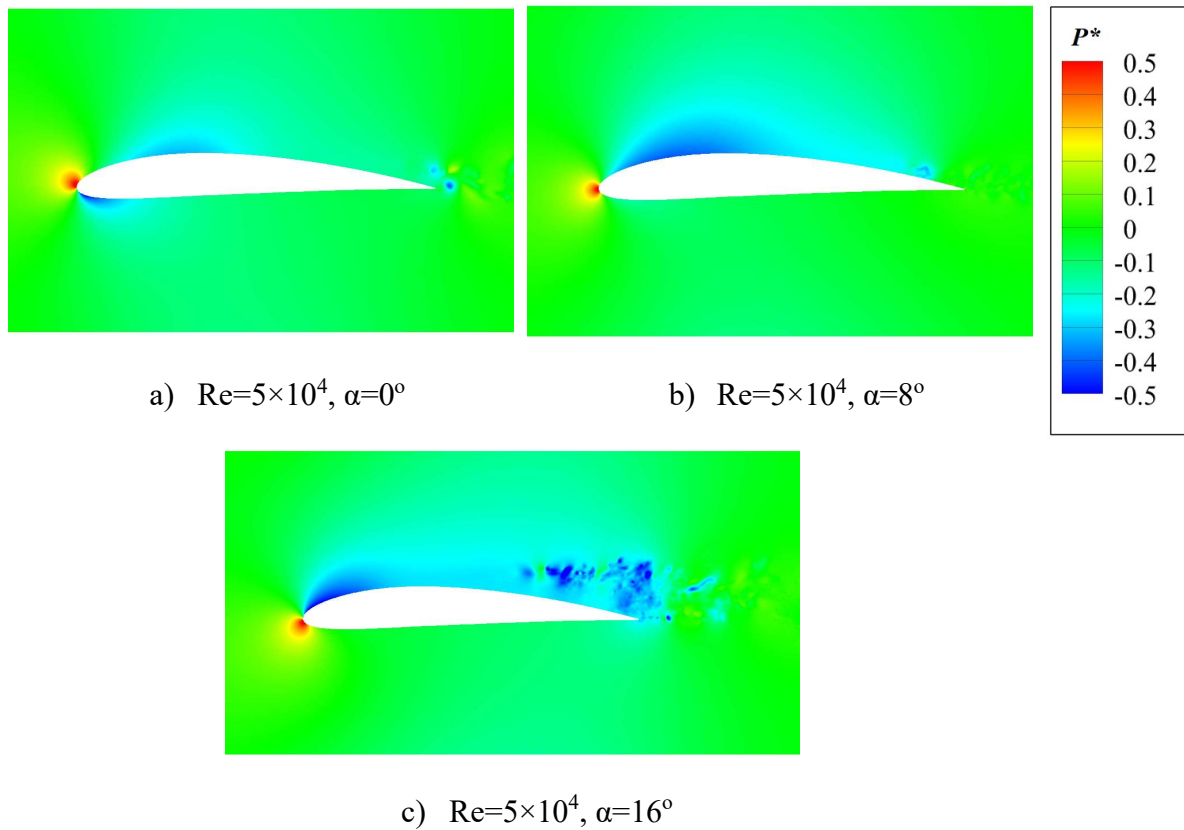
**Fig. 7** Isosurface contours of the spanwise vorticity over the NACA-4412 airfoil at different Reynolds numbers and AoAs.

**Table 2** Separation point on the surface of the wind turbine section for different Re and AoAs

Re	AoA ( $\alpha^\circ$ )	$X_{sep}/C$
50,000	0	0.58
	8	0.25
	16	0.19
75,000	0	0.39
	8	0.20
	16	0.17
150,000	0	0.30
	8	0.17
	16	0.14

Figure 8 demonstrates the instantaneous dimensionless pressure contour around the aerofoil at different angles of attack at the Reynolds number of  $5 \times 10^4$ . Generally, the highest pressure is seen in the vicinity of the leading edge where the relative velocity has interactions with the blade. Depending on the angle of attack, the pressure distributions on the aerofoil surfaces vary. At the angle of attack of 0 degree, the low-pressure fields are noticed on both surfaces with some pressure bubbles leaving from the trailing edge of the blade. Raising the angle of attack increases the pressure difference between the two surfaces, which introduces the lift. However, at  $\alpha=16^\circ$ , the flow separation becomes very large as it lies within the post-stall region. As a

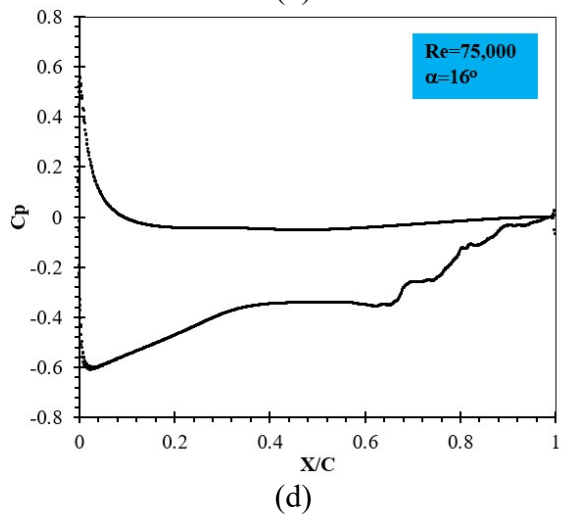
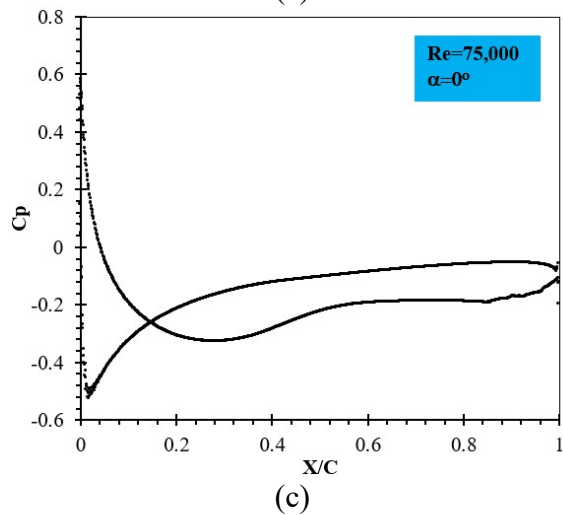
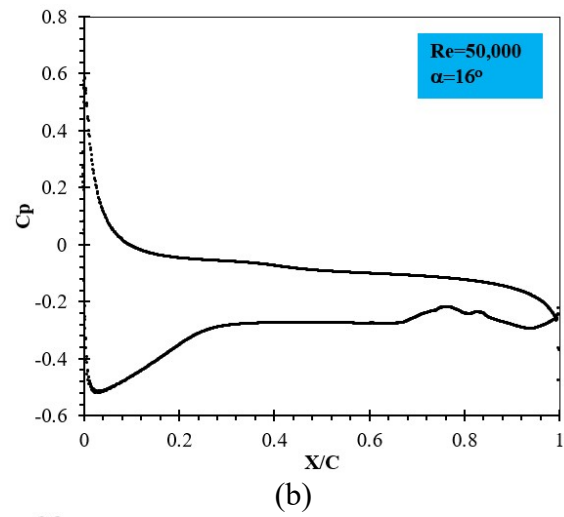
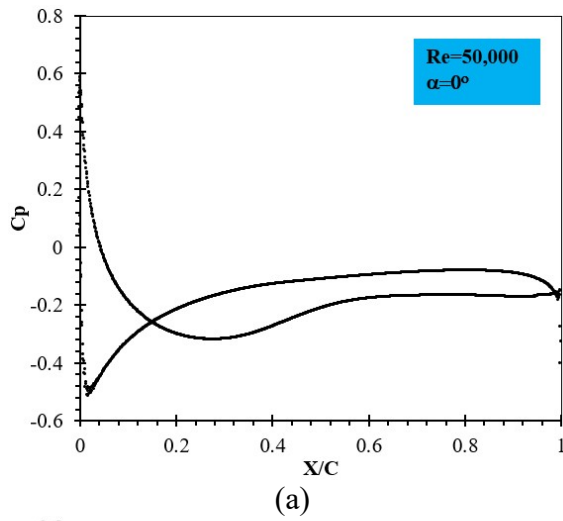
result, pressure fluctuations are detected on the suction surface and pressure bubbles are formed in the separation zone.

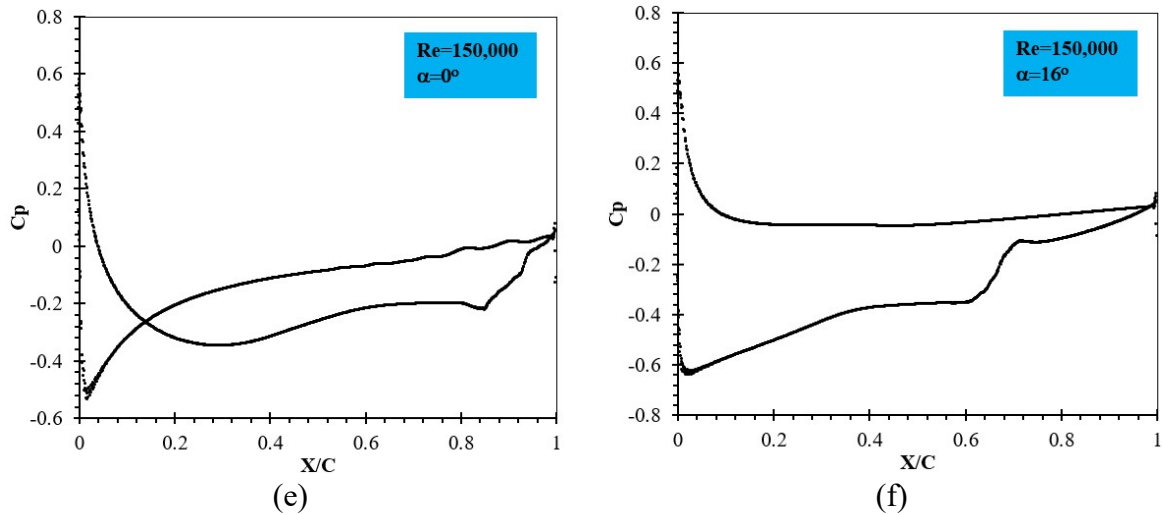


**Fig. 8** Instantaneous Pressure contours over the blade for different angle of attacks at  $Re=5 \times 10^4$ .

Figure 9 illustrates the time-averaged pressure coefficients on both pressure and suction surfaces at different angles of attack and Reynolds numbers. At the Reynolds number of  $5 \times 10^4$ , the pressure difference between the two surfaces is very small at the angle of attack of 0 degree, which results in a small lift. At  $\alpha=16^\circ$ , the pressure difference between the two surfaces is larger than that of the 0-degree angle of attack; however, some pressure fluctuations are seen on the suction surface nearby the trailing edge due to the flow separation and formation of separation bubbles. This phenomenon can be visualised in Fig. 6 (c). Although a similar trend in pressure coefficient distribution is observed at the angle of attack of 0 degree at the Reynolds numbers of  $5 \times 10^4$  and  $7.5 \times 10^4$ , some pressure variations are introduced near the trailing edge if the

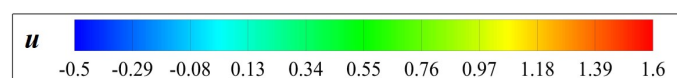
Reynolds number is increased to  $7.5 \times 10^4$ . The pressure fluctuations near the trailing edge become stronger when raising the angle of attack to 16 degrees, and they are also stronger than that of the Reynolds number of  $5 \times 10^4$ . Due to a higher wind speed at the Reynolds number of  $1.5 \times 10^5$ , pressure deviations are observed at both angles of attack; however, the deviation is more significant at  $\alpha=16^\circ$ . Therefore, it is now understood from the results obtained that increasing Reynolds number can reduce the size of flow separation and delay the stall phenomenon; however, at the same time, it imposes unsteady pressure fluctuations to the aerofoil surfaces due to stronger vortex generation.

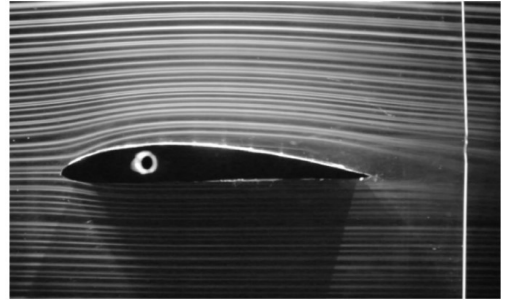
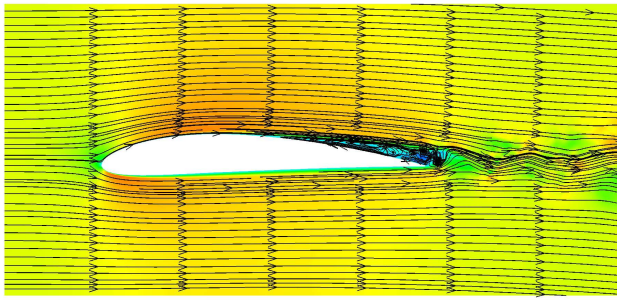




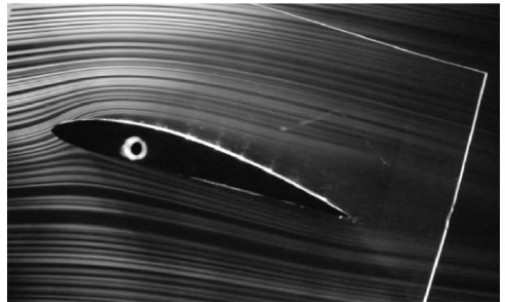
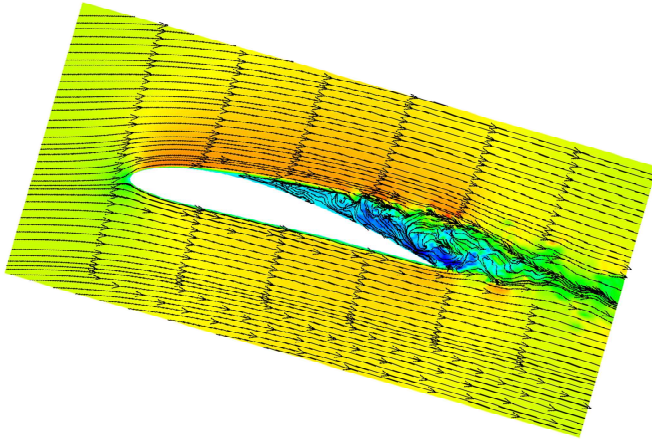
**Fig. 9** Time-averaged pressure coefficient profiles over the wind turbine airfoil section at different Re numbers and AoAs

The comparisons of the flow streamlines obtained from the experiment and the present DNS simulation at different angles of attack and Reynolds number are presented in Figure 10. It is seen that the present DNS simulation accurately predicted the flow separation and flow behaviour at all angles of attack at different Reynolds numbers. Therefore, it can be noted that the present DNS simulation is accurate and can be reliably used to predict the unsteady flow nature. Interestingly, the DNS simulation can provide more detailed flow information compared to the experiment. Flow recirculation and vortex generation in the separation zone as well as the laminar to turbulence transition process can be clearly observed and identified with the DNS simulation. However, it is very difficult or impossible to obtain these flow details through the experiment or other low-fidelity numerical models such Reynolds Averaged Navier-Stokes (RANS) models. Therefore, this can be marked as one of the novelties of the present DNS simulation, and the flow behaviours and information obtained from this paper can be used as references for validation of the numerical models.

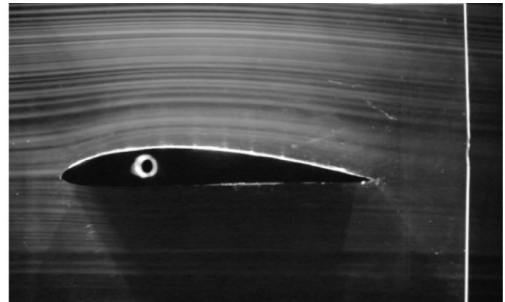
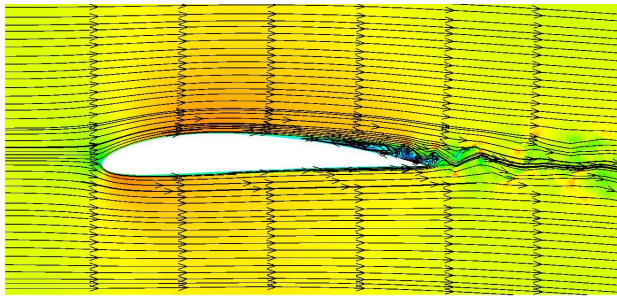




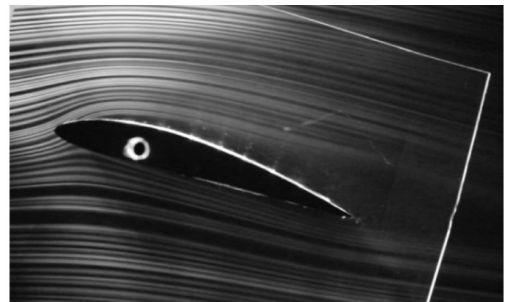
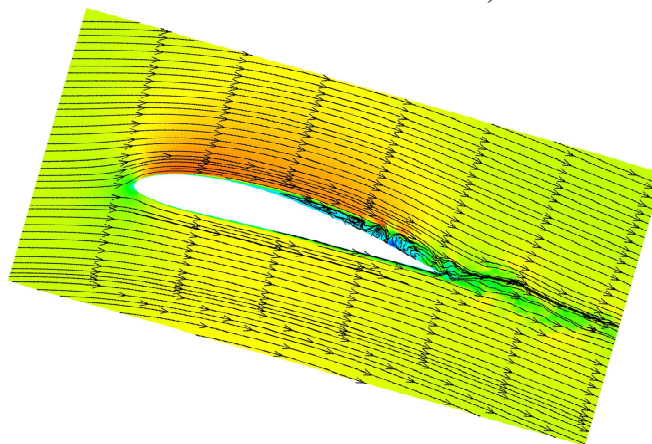
a)  $Re=5 \times 10^4, \alpha=0^\circ$



b)  $Re=5 \times 10^4, \alpha=16^\circ$



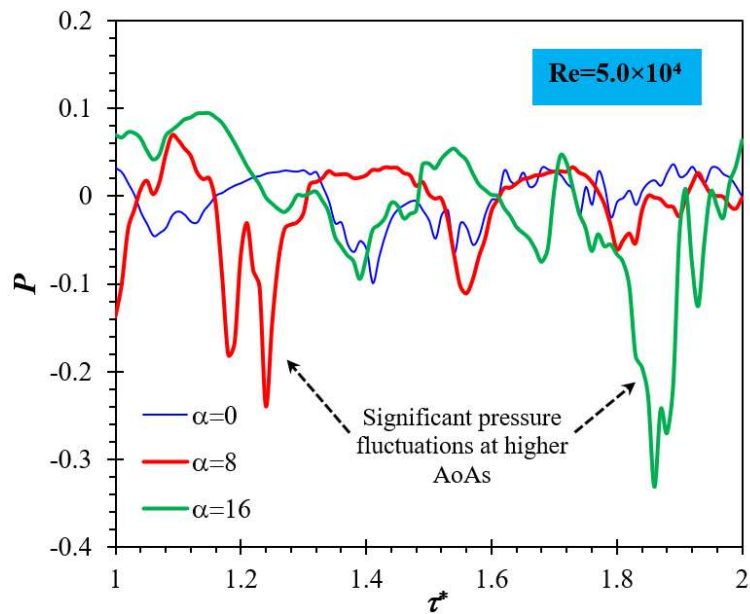
c)  $Re=7.5 \times 10^4, \alpha=0^\circ$



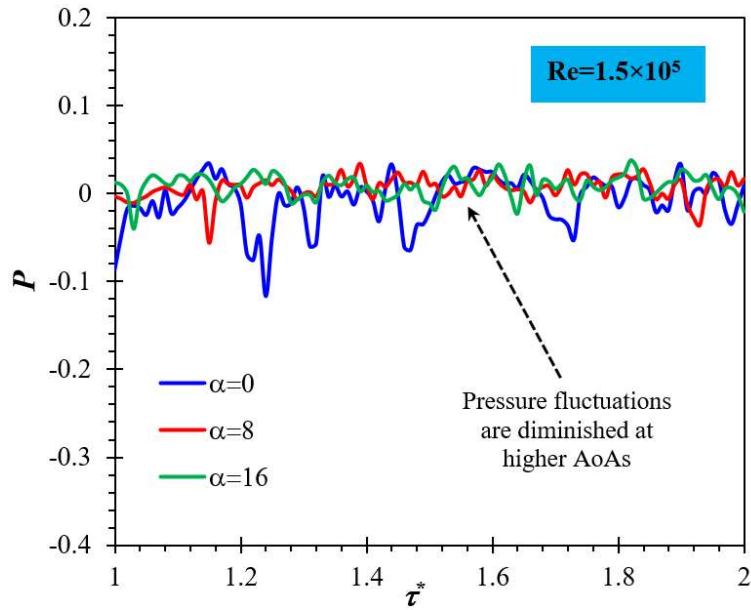
d)  $Re=7.5 \times 10^4, \alpha=16^\circ$

**Fig. 10** Comparison between the DNS results with experiments [6] for the instantaneous flow streamlines over the wind turbine blade section.

The variations of pressure fluctuations in the wake region of the wind turbine blade at the relatively lower and higher Reynolds numbers are shown in Figure 11. At the Reynolds number of  $5 \times 10^4$ , significant pressure fluctuations are detected at higher angle of attacks and the frequencies of pressure fluctuations are smaller at lower angles of attack. In contrast to the Reynolds number of  $5 \times 10^4$ , the pressure fluctuations are diminished at higher angles of attack and the frequencies are also smaller at greater values of the angle of attack. It is understood that this is another novelty of the present DNS simulation as it can provide the unsteady nature of the flow in the wake region in detail while this cannot be obtained with other low-fidelity numerical models.



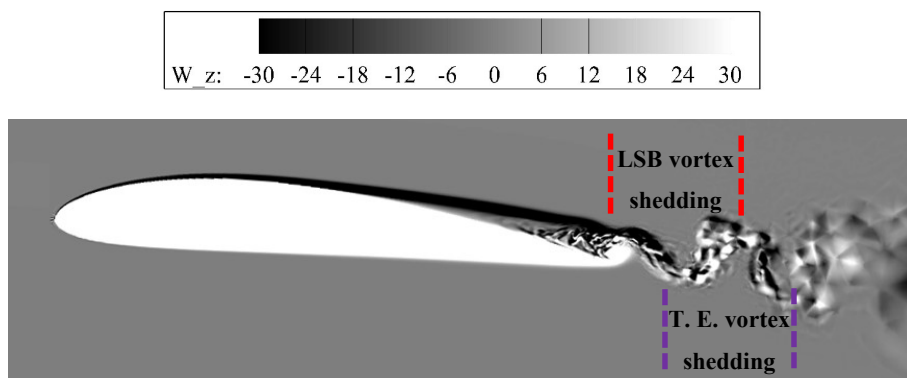
a) Re=50,000



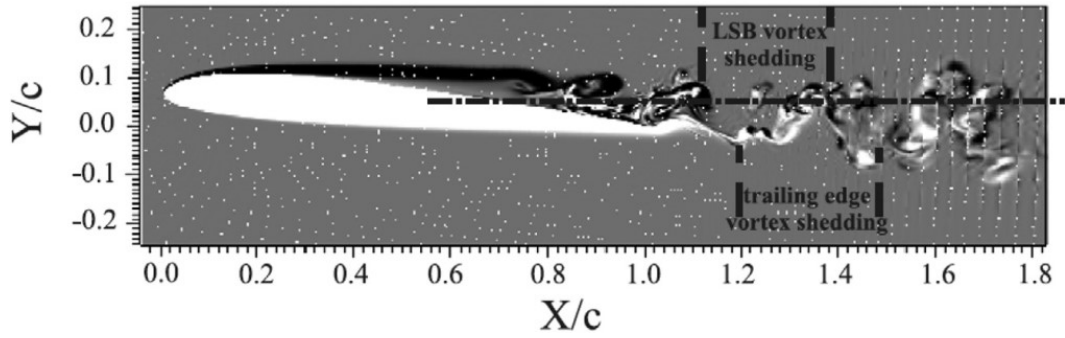
b)  $Re=150,000$

**Fig. 11** The variations of the pressure fluctuations in the wake region of the WT blade

Figure 12 compares the vortex shedding from the aerofoil between the experiment and the present DNS simulation. The vortex structures at  $\alpha=4^\circ$  and Reynolds number of  $2.5 \times 10^4$  are presented in this figure. Two classifications of vortex shedding due to LSB and trailing edge separation are identified in the vortex shedding process, and they can be clearly seen above the aerofoil and in the wake region. As seen, the present DNS simulation accurately identified both LSB and trailing edge vortex shedding, and they are consistent with the experiment.



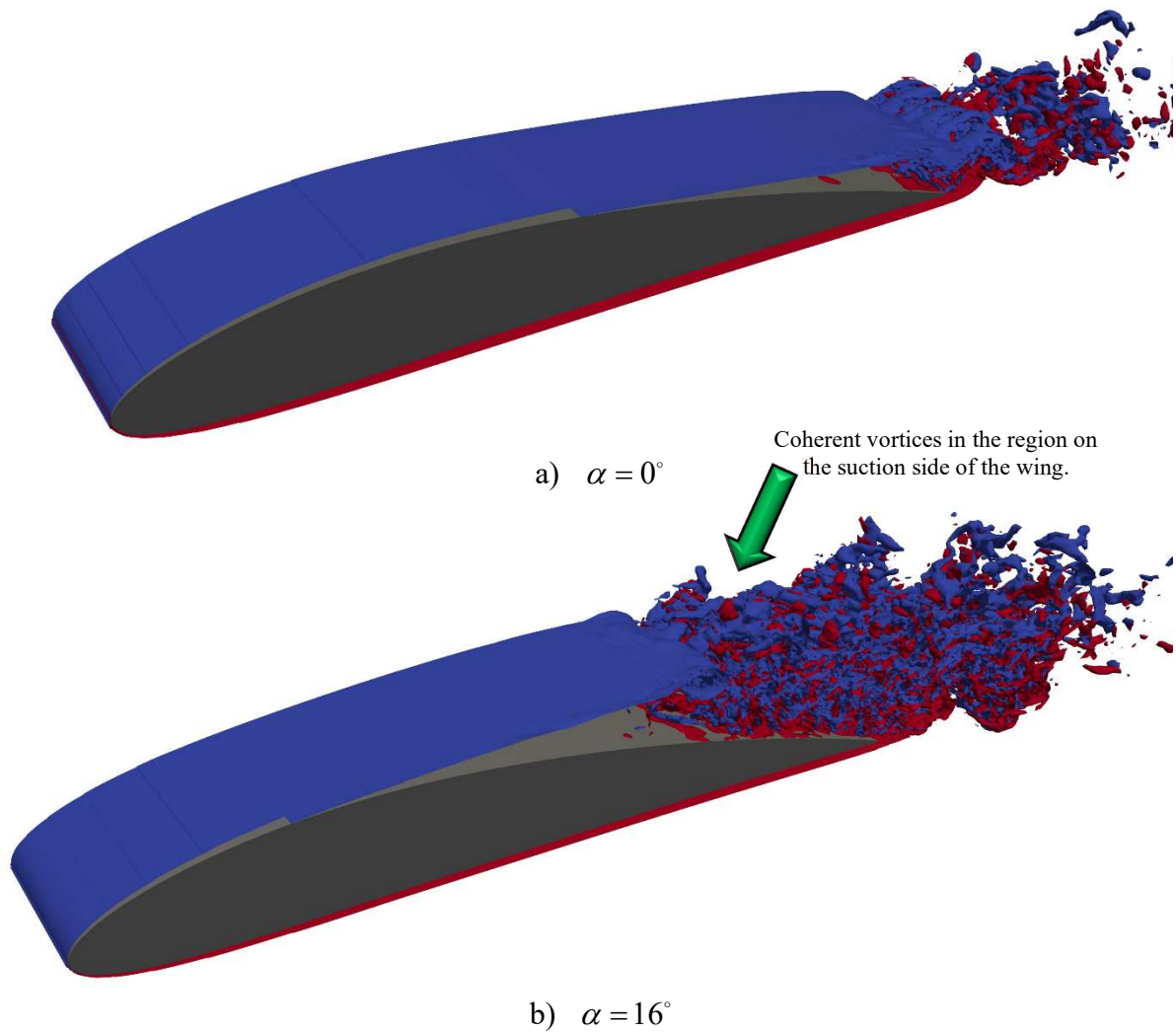
a) Present study, DNS,  $Re=2.5 \times 10^4$ ,  $\alpha=4^\circ$



b) Experimental visualisation [34]

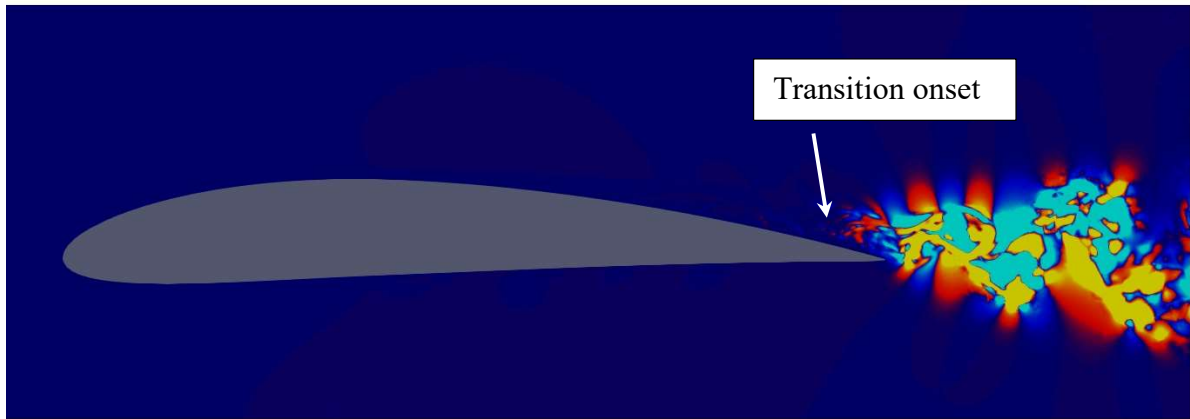
**Fig. 12** Comparison of vorticity contours of DNS with experiments

Figure 13 plots the instantaneous spanwise vorticity field for the angles of attack of 0 degree and 16 degrees at the Reynolds number of  $5 \times 10^4$ . This figure not only provides the vorticity structures in the spanwise direction but also highlights the laminar to turbulence transition process based on relatively low and high angles of attack. Generally, as the flow past the aerofoil surfaces, the flow becomes unsteady and separates at certain point depending on the angle of attack and the curvature of the aerofoil. The flow separation generates the separated shear layers which then roll up and break down into smaller vortex structures as the flow develops downstream. Finally, the flow becomes fully turbulent and vortex shedding occurs downstream of the trailing edge of which the vortex structures are similar to those of Karman vortex. The vorticity field is almost uniform in the spanwise direction. The effect of the angle of attack on the laminar to turbulence transition process can be seen in this figure. The flow disturbances due to the separated shear layers and vortex generation are amplified by the large flow separation when the angle of attack is increased to 16 degrees, which cause the flow to be more unsteady and turbulent.

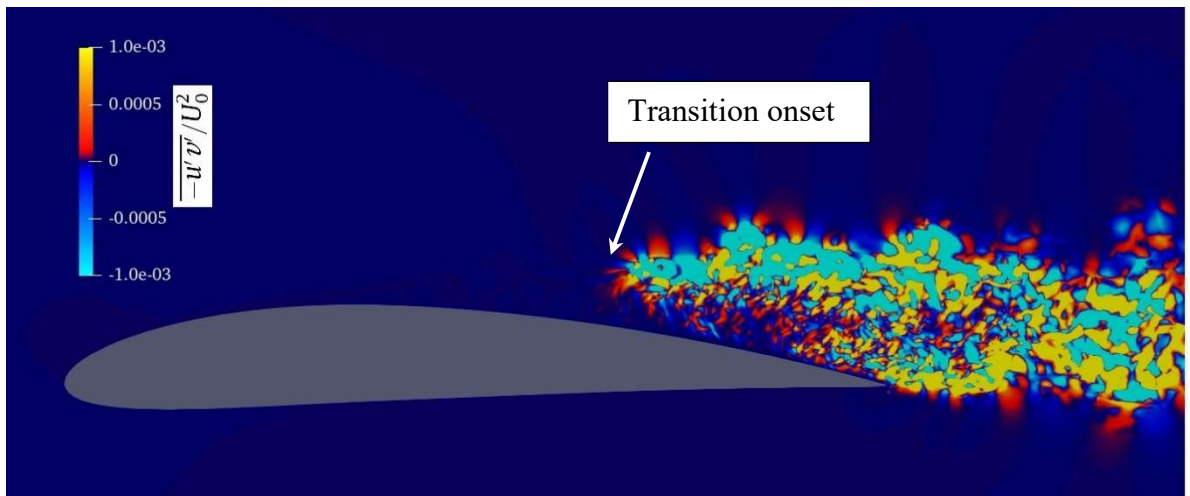


**Fig. 13** Instantaneous spanwise vorticity field plotted at  $Re=50,000$  for  $w_z=\pm 30$ .

The transition onset can be identified and indicated by means of the mean Reynolds stress. The distributions of the mean Reynolds stress,  $-\overline{u'v'}/U_0^2$ , over the aerofoil at the angles of attack of 0 degree and 16 degrees at the Reynolds number of  $5 \times 10^4$  is presented in Figure 14. The threshold value of 0.0001 is plotted to indicate the transition onset. As shown, the transition happens in the separated shear layer and the location of the transition onset depends on the angle of attack. A strong concentration of Reynolds stress can be seen downstream of the trailing edge at the angle of attack of 0 degree whereas it can be observed after the transition occurs on the suction surface at the 16-degree angle of attack. The large structures break down into smaller ones as the turbulence develops downstream.



a)  $Re=50,000, \alpha=0^\circ$



b)  $Re=50,000, \alpha=16^\circ$

**Fig. 14** Distributions of the mean Reynolds stress  $\frac{-u'v'}{U_0^2}$  over the NACA-4412 blade (The transition onset is indicated by the threshold value 0.0001).

The instantaneous velocity profiles in the wake region of the NACA-4412 airfoil at  $Re=50,000$  are presented in Figure 15. The dimensionless wake profiles ( $u/U_0$ ) are plotted over the line between points A (1.2,-0.3,0.1), and B (1.2,0.3,0.1) with a distance of  $x=0.2$  from the trailing edge of the wind turbine mid-section blade. The results show that strong fluctuations and back flows are generated in the wake region of the airfoils with high angle of attacks ( $\alpha = 16^\circ$ ). As discussed earlier, the strong vortex generation and recirculation flows over the blades with high angle of attacks is the main reason for the fluctuations in the air flow velocity in this region.

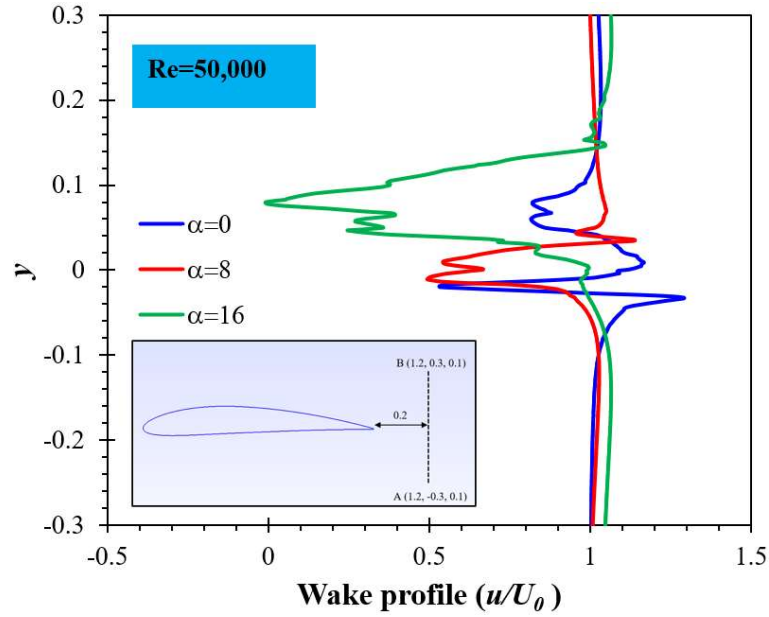


**Fig. 15** Instantaneous velocity profiles in the wake region over the wind turbine airfoil at  $Re=50,000$  for different AoAs.

Figure 16 depicts the impacts of polynomial-order on the power spectral density (PSD) in the wake region. According to the averaging periodograms model, the pressure signals at various time steps are divided in divisions with 50% similarity between them. The specifics of this technique can be found in Ref. [35]. The PSD of the variable  $F$  is defined by [35]:

$$PSD(St) = \frac{2(\hat{J})^2}{\Delta f C/U} = \frac{2(\hat{J})^2}{\Delta(St)} \quad (9)$$

where  $St=fC/U$ ,  $f$  and  $C$  are the Strouhal number, frequency, and the chord of the airfoil, respectively.  $\hat{J}$  indicates the amplitude that can be calculated by doing Fourier transform of signals. It is seen that the numerical findings have convergency, and PSD values drop under of the  $-5/3$  line. The results show that converging of the results over wind turbine blade with  $P=12$  is delayed in comparison with the same NACA-4412 wind turbine airfoil blade with  $P=8$ . It is due to the more computational time and higher CFL number for the case of  $P=12$ . It can be seen that both of the cases are convergent and the selected time steps are appropriate for the computations over the NACA-4412 airfoil blade with  $N_{pt}=48$  and  $L_z=0.5$ .

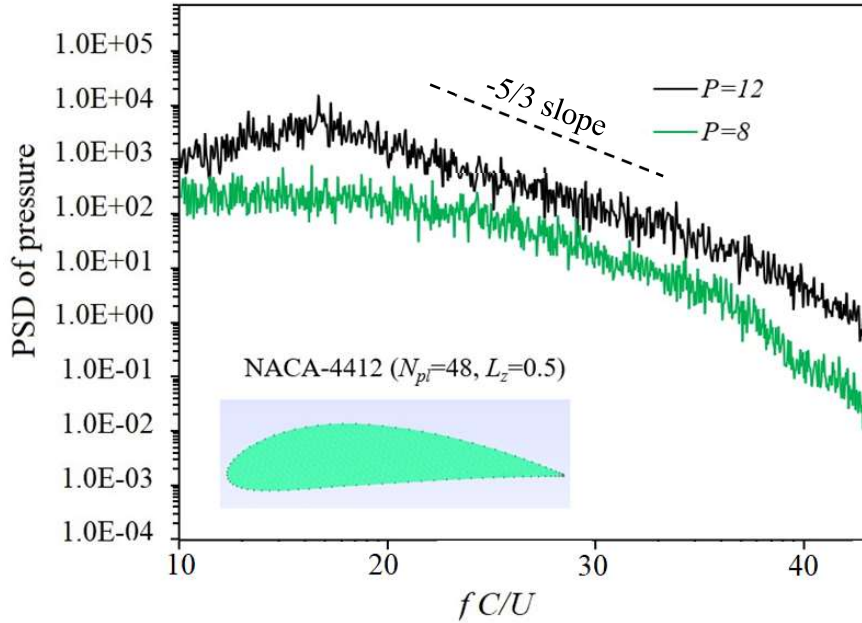


**Fig. 16** Spanwise power spectra of pressure signals against Strouhal number taken at probes right downstream of the airfoil trailing edge.

#### 4. Conclusions

In this paper, direct numerical simulations of the transient flow past a section of a wind turbine blade are conducted based on NACA4412 aerofoil to investigate the flow structures and the laminar separation bubbles over the aerofoil surfaces at different angles of attack and wide ranges of Reynolds number. The main findings of the present study are as follows:

- The Drag-Lift coefficients were compared with the experiment to ensure the accuracy of the present simulation on calculating the forces acting on the aerofoil surfaces. It is found that raising Reynolds number could delay the stall.
- Comparison between the numerical results and the experiments for the flow structure and vortex generation revealed that the present DNS simulation accurately captured the flow structures as they are similar to those of the experiment. Previous numerical models were not able to capture the instantaneous pressure fluctuations over wind turbine blades, which cannot be obtained with other low-fidelity numerical models.

- Flow separation points are accurately predicted in the present DNS simulations, which show that flow separation points move towards the leading edge as the angle of attack increases whereas they move in the direction of the trailing edge when increasing Reynolds numbers.
- Two classifications of vortex shedding such as LSB vortex shedding and trailing edge vortex shedding are identified, which is also consistent with the experiment. Visualisation of the vortex structures on the aerofoil surfaces show that strong vortex generation and flow recirculation are observed in the flow separation zone at  $\alpha=16^\circ$  when the Reynolds number is  $5 \times 10^4$ .
- The size of separation is reduced if the Reynolds number is increased. It is also observed that vortex structures and vortex shedding frequencies are smaller at higher Reynolds number. However, increasing Reynolds number imposes higher pressure fluctuations on the suction surface of the aerofoil. The fluctuations are more significant at higher Reynolds numbers.

### **Acknowledgment**

The authors would like to acknowledge the financial support received from Engineering Physics and Science Research Council of UK (EPSRC EP/R010633/1).

### **References**

- [1] S.W. Naung, M. Rahmati, H. Farokhi, Nonlinear frequency domain solution method for aerodynamic and aeromechanical analysis of wind turbines, *Renewable Energy*, (2020).
- [2] S. Win Naung, M. Rahmati, H. Farokhi, Aeromechanical Analysis of a Complete Wind Turbine Using Nonlinear Frequency Domain Solution Method, *Journal of Engineering for Gas Turbines and Power*, (2020).

- [3] S. Win Naung, M. Rahmati, H. Farokhi, Aeromechanical Analysis of Wind Turbines Using Non-Linear Harmonic Method, International Conference on Offshore Mechanics and Arctic Engineering, American Society of Mechanical Engineers, 2019, pp. V010T009A060.
- [4] T.-t. Zhang, M. Elsakka, W. Huang, Z.-g. Wang, D.B. Ingham, L. Ma, M. Pourkashanian, Winglet design for vertical axis wind turbines based on a design of experiment and CFD approach, *Energy Conversion and Management*, 195 (2019) 712-726.
- [5] W. Huang, H. Wu, Y.-g. Yang, L. Yan, S.-b. Li, Recent advances in the shock wave/boundary layer interaction and its control in internal and external flows, *Acta Astronautica*, 174 (2020) 103-122.
- [6] K. Koca, M.S. Genç, H.H. Açıknel, M. Çağdaş, T.M. Bodur, Identification of flow phenomena over NACA 4412 wind turbine airfoil at low Reynolds numbers and role of laminar separation bubble on flow evolution, *Energy*, 144 (2018) 750-764.
- [7] W. Xu, G. Li, F. Wang, Y. Li, High-resolution numerical investigation into the effects of winglet on the aerodynamic performance for a three-dimensional vertical axis wind turbine, *Energy Conversion and Management*, 205 (2020) 112333.
- [8] T. Zhang, Z. Wang, W. Huang, D. Ingham, L. Ma, M. Pourkashanian, A numerical study on choosing the best configuration of the blade for vertical axis wind turbines, *Journal of Wind Engineering and Industrial Aerodynamics*, 201 (2020) 104162.
- [9] H.H. Açıknel, M.S. Genc, Control of laminar separation bubble over wind turbine airfoil using partial flexibility on suction surface, *Energy*, 165 (2018) 176-190.
- [10] Y. Kamada, T. Maeda, J. Murata, Y. Nishida, Visualization of the flow field and aerodynamic force on a Horizontal Axis Wind Turbine in turbulent inflows, *Energy*, 111 (2016) 57-67.

- [11] M. Ou, L. Yan, W. Huang, S.-b. Li, L.-q. Li, Detailed parametric investigations on drag and heat flux reduction induced by a combinational spike and opposing jet concept in hypersonic flows, *International Journal of Heat and Mass Transfer*, 126 (2018) 10-31.
- [12] W. Huang, W.-d. Liu, S.-b. Li, Z.-x. Xia, J. Liu, Z.-g. Wang, Influences of the turbulence model and the slot width on the transverse slot injection flow field in supersonic flows, *Acta Astronautica*, 73 (2012) 1-9.
- [13] A. Rezaeiha, H. Montazeri, B. Blocken, Active flow control for power enhancement of vertical axis wind turbines: Leading-edge slot suction, *Energy*, 189 (2019) 116131.
- [14] V. D'Alessandro, G. Clementi, L. Giammichele, R. Ricci, Assessment of the dimples as passive boundary layer control technique for laminar airfoils operating at wind turbine blades root region typical Reynolds numbers, *Energy*, 170 (2019) 102-111.
- [15] S. Moriguchi, H. Miyazawa, T. Furusawa, S. Yamamoto, Large Eddy Simulation of a Linear Turbine Cascade with a Trailing Edge Cutback, *Energy*, (2020) 119694.
- [16] S.W. Naung, M. Rahmati, H. Farokhi, Direct Numerical Simulation of Interaction between Transient Flow and Blade Structure in a Modern Low-Pressure Turbine, *International Journal of Mechanical Sciences*, 192 (2020) 106104.
- [17] A. Saleem, M.-H. Kim, Effect of rotor tip clearance on the aerodynamic performance of an aerofoil-based ducted wind turbine, *Energy Conversion and Management*, 201 (2019) 112186.
- [18] A. Cassinelli, H. Xu, F. Montomoli, P. Adami, R. Vazquez Diaz, S.J. Sherwin, On the effect of inflow disturbances on the flow past a linear LPT vane using spectral/hp element methods, *Turbo Expo: Power for Land, Sea, and Air*, American Society of Mechanical Engineers, 2019, pp. V02CT41A032.

- [19] A. Rezaeiha, H. Montazeri, B. Blocken, Characterization of aerodynamic performance of vertical axis wind turbines: impact of operational parameters, *Energy Conversion and Management*, 169 (2018) 45-77.
- [20] R. Mereu, S. Passoni, F. Inzoli, Scale-resolving CFD modeling of a thick wind turbine airfoil with application of vortex generators: Validation and sensitivity analyses, *Energy*, 187 (2019) 115969.
- [21] R. Wahidi, W. Lai, J.P. Hubner, A. Lang, Volumetric three-component velocimetry and PIV measurements of Laminar Separation Bubbles on a NACA4412 Airfoil, 16th Int. Symp of applications of laser techniques of fluid mechanics, 2012.
- [22] W. Cui, Z. Xiao, X. Yuan, Simulations of transition and separation past a wind-turbine airfoil near stall, *Energy*, (2020) 118003.
- [23] M. O'meara, T.J. Mueller, Laminar separation bubble characteristics on an airfoil at low Reynolds numbers, *AIAA journal*, 25 (1987) 1033-1041.
- [24] M. Alam, N.D. Sandham, Direct numerical simulation of short laminar separation bubbles with turbulent reattachment, *Journal of Fluid Mechanics*, 410 (2000) 1-28.
- [25] G. Karniadakis, S. Sherwin, *Spectral/hp element methods for computational fluid dynamics*, Oxford University Press 2013.
- [26] S.J. Sherwin, M. Ainsworth, Unsteady Navier–Stokes solvers using hybrid spectral/hp element methods, *Applied Numerical Mathematics*, 33 (2000) 357-363.
- [27] D. Moxey, C.D. Cantwell, Y. Bao, A. Cassinelli, G. Castiglioni, S. Chun, E. Juda, E. Kazemi, K. Lackhove, J. Marcon, Nektar++: Enhancing the capability and application of high-fidelity spectral/hp element methods, *Computer Physics Communications*, 249 (2020) 107110.
- [28] Y. Bao, R. Palacios, M. Graham, S. Sherwin, Generalized thick strip modelling for vortex-induced vibration of long flexible cylinders, *Journal of Computational Physics*, 321 (2016) 1079-1097.

- [29] A. Cassinelli, P. Adami, F. Montomoli, S.J. Sherwin, On the effect of wake passing on a low pressure turbine cascade using spectral/hp element methods, *Bulletin of the American Physical Society*, 64 (2019).
- [30] M.E. Nakhchi, S.W. Naung, M. Rahmati, DNS of secondary flows over oscillating low-pressure turbine using spectral/hp element method, *International Journal of Heat and Fluid Flow*, 86 (2020) 108684.
- [31] C.D. Cantwell, D. Moxey, A. Comerford, A. Bolis, G. Rocco, G. Mengaldo, D. De Grazia, S. Yakovlev, J.-E. Lombard, D. Ekelschot, Nektar++: An open-source spectral/hp element framework, *Computer physics communications*, 192 (2015) 205-219.
- [32] G.E. Karniadakis, M. Israeli, S.A. Orszag, High-order splitting methods for the incompressible Navier-Stokes equations, *Journal of computational physics*, 97 (1991) 414-443.
- [33] J.-L. Guermond, J. Shen, Velocity-correction projection methods for incompressible flows, *SIAM Journal on Numerical Analysis*, 41 (2003) 112-134.
- [34] A. Ducoin, J.-C. Loiseau, J.-C. Robinet, Numerical investigation of the interaction between laminar to turbulent transition and the wake of an airfoil, *European Journal of Mechanics-B/Fluids*, 57 (2016) 231-248.
- [35] M.A. Alhawwary, Z.J. Wang, DNS and LES of the flow over the T106C turbine using the high-order FR/CPR method, *AIAA Scitech 2020 Forum*, 2020, pp. 1572.